

CHALMERS



Finding the Jeffrey Orbits

Master's Thesis in Complex Adaptive Systems

Staffan Ankardal

Department of Physics & Engineering Physics
Non-linear Dynamics & Statistical Physics
CHALMERS UNIVERSITY OF TECHNOLOGY
Gothenburg, Sweden 2013
Master's Thesis 2013:1

Abstract

The Jeffery orbits define the motion of axissymmetrical particles in shear flow and is thus important in the study of suspensions of particles. In this thesis I attempt to verify the equations of motion experimentally using glass particles in a reversible flow in a microfluidic PDMS channel and an optical tweezer. An automatic tracking of the particles was developed and a number of improvements were made compared to previous experiments such as by Einarsson et al[13]. We study the effects of asymmetry on the particles and the transition from periodic to quasi-periodic orbits for different initial conditions of particles and for different degrees of asymmetry. A good match with theoretical results is found for some measurements, but there are some unexplained behaviours when the flow is reversed.

Acknowledgements

I hereby wish to thank my Supervisors Bernhard Mehlig and Dag Hanstorp for helping me through this journey. I want to thank girlfriend Callie Gibbons for supporting me through the work on this thesis and Alexander Laas for being a tireless and understanding co-worker. I want to thank all the contributors to the wealth of open source software which I have used to create everything from most of the software to more of the figures and of course this very report.

Staffan Ankardal, Göteborg Sweden INSERT PROPER DATE 3/11/13

Contents

1	Introduction	1
1.1	Introduction	1
1.1.1	Background	1
2	Theory	4
2.1	Fluid Dynamics	4
2.1.1	Navier Stokes	5
2.1.2	Reynold's Number	5
2.1.3	Stokes Drag and Stokes's law	6
2.2	Euler Angles and our Coordinate System	7
2.2.1	Triaxial particles	9
2.3	Jeffery Orbits	10
2.3.1	Winding Number	13
3	Method	16
I	Improvements of Experimental Setup	17
3.1	Improvements	19

3.1.1	Particles and Channel	19
3.1.2	Automated Tracking	22
3.1.3	Aquiring the image	22
3.1.4	Removing noise	22
3.1.5	Contour detection and selection	23
3.1.6	Adjusting the Camera velocity	23
3.1.7	Time Considerations	24
3.2	Experimental Setup	24
3.2.1	List of equipment	27
3.2.2	Density matching	27
II	Measurements and Analysis	28
3.3	Data Analysis	29
3.3.1	Particle identification	29
3.3.2	Estimation of orientation	30
3.3.3	Width compensation	31
3.3.4	brushing	32
3.3.5	Winding number estimation	33
3.3.6	Matching to theoretical orbit	34
4	Results	35
4.1	Particle A	36
4.2	Particle B	40
4.2.1	Run 1	40
4.2.2	Run 2	42
5	Discussion	45
A	Raw data	46

1

Introduction

1.1 Introduction

My goal in this thesis is to study and better understand the dynamics of ellipsoidal particles in shear flow, and is a continuation of two previous masters theses [1, 2]. This is done by analysing micrometer length glass particles in a shear flow and comparing this to theoretical models. Before discussing either of these processes more in depth some background and basic theory is needed.

1.1.1 Background

Understanding the dynamics of particles in flow might appear somewhat esoteric but there is actually a number of topics where it is important. In fluid dynamics non-newtonian fluids are often high concentrations of particles suspended in liquid, such ketchup or blood, and understanding this behaviour might need an improved understanding of how each individual particle will behave. In medical applications understanding the dynamics of ellipsoidal particles like bacteria can be relevant to a detailed understanding of their interactions with cells and other bodies as discussed by Tolga et al[11]. So if we accept that it is a topic worth studying the next question is how much do we already know.

1.1. INTRODUCTION

The study of particle dynamics in flow began with Einstein's paper from 1905 [3] in which he showed how much the suspended spherical particle would increase the viscosity of a fluid. Jeffrey in his 1922 paper [4] extended these results to ellipsoidal axis-symmetrical ellipsoidal particles and derived equations for the orientational dynamics of the particles, in other words how the particles would rotate as a function of time. For systems where inertial effects could be discarded the motion was found to be periodic and depending only on the initial condition of the particle.

Developments on triaxial particles, started with Gierszewski & Chaffey (1978)[5] and was continued by Hinch & Leal (1979)[6] and more recently by Yarin et al in 1993[7]. The dynamics found for axis-symmetric particles by Jeffrey were periodic, but it was shown by Hinch & Leal that some orbits would be doubly periodic, in other words following two separate independent periods. This behaviour will primarily be referred to as quasi-periodic from here-on out.

Yarin then was able to use numerical simulations to generate a surface of section [8] for some asymmetric relations between the two minor axes showing that not only was there double periodic or quasi periodic orbits but for sufficiently large asymmetries there would be chaotic orbits. Several other surfaces of section were also produced by Johansson (2012)[1] using the same method as Yarin with higher resolution thanks to improvements in computing power. It was shown that only very small asymmetries on the order of 1% will lead to quasi-periodic motion for some initial conditions.

Attempts to experimentally verify these theoretical results were first done by Goldsmith and Mason in 1962[9] who used flow in a glass pipe to observe the rotation rate for several different particle shapes. He was able to confirm that the rotation rate matched well with that predicted from Jeffery orbits but he did not study the actual orbits. Since then most experimental research, such as by Harlen and Koch[10] has been focused on the effect diluted suspensions of particles have on the properties of a liquid. Only tangential efforts such as by Tolga[11] were concerned with the Jeffery orbits. A good summary of both theoretical and experimental results was written by Petrie in 1999 [12].

The first dedicated experiments to measure the actual Jeffery orbits in angular components and verify the orientational dynamics was done by Einarsson et al [13] in 2011. Although there was some promising results, the vast majority of particles were asymmetric to the point of chaotic or

1.1. INTRODUCTION

highly quasi-periodic. Moreover the width and length of particles both varied great and could not be measured with good accuracy, meaning that the aspect ratio could not accurately be determined. This mean that although the orbits could be qualitatively shown to be similar to some Jeffery orbits no particular particle could be shown to exhibit both quasi periodic and periodic motion, and there was no particle that could be well matched to a particular orbit. There was also quite few particles that showed a perfectly identical reversal through the entire length of the channel when the flow was reversed.

The goal now is to experimentally verify the results of [6, 7] and show that the same particle will show different types of motion for different initial conditions and furthermore that different particles will also show different motion for the same initial conditions based on the asymmetry. To do this we will study orientation of a micrometer length particle in a creeping shear flow. To verify that the flow is a creeping flow we will show that the dynamics revert as the flow is reverted. The results for different initial conditions will then be compared to theoretical predictions.

2

Theory

In order to better understand the results and discussions in this thesis some rather basic results in fluid dynamics, image analysis and other fields need to be understood by the reader.

1) It is however not the focus of this thesis and as such I will try to be as brief as possible, and an experienced reader can safely skip to the next chapter.

OR

2) As the focus of this thesis is experimental I will not go into great detail, but try to briefly motivate and quickly summarize results, and refer the inquisitive reader to more thorough sources. As no recent developments are discussed, readers comfortable in these fields can skip this chapter without any loss in understanding.

2.1 Fluid Dynamics

In order to understand the motivations, limitations and behaviour of the experiment we need to know about a few key concepts in fluid dynamics.

2.1.1 Navier Stokes

2.1.2 Reynold's Number

The Reynolds number (Re) is a dimensionless number describing the ratio of inertial forces to viscous forces in a flow. For flow in a pipe it is defined as [14]

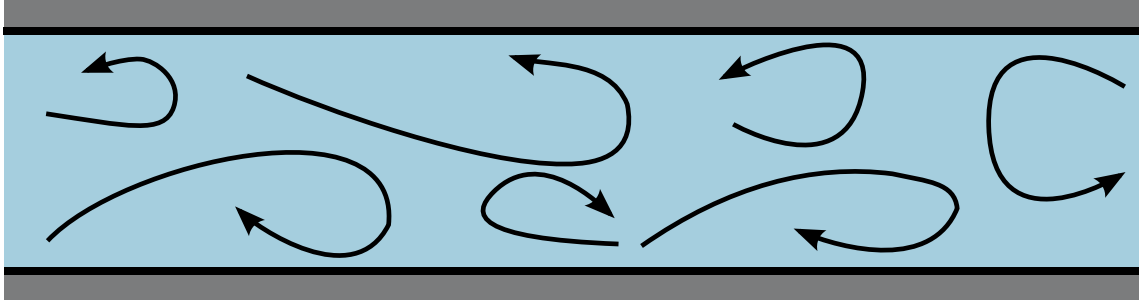
$$Re = \frac{UL\rho}{\mu} \quad (2.1)$$

where U is the characteristic velocity of the flow, L is the characteristic length, ρ is the density and μ is the dynamic viscosity. This is used to estimate the 'regime' of the flow, of which there are two primary types.

1. Laminar flow, where viscous forces dominate over inertial forces
2. Turbulent regime where inertial forces dominate.

The Reynolds number is a ratio between the inertial forces and viscous forces so we get more turbulent flow for larger Reynolds numbers, a simple visual characterization of the flow types can be seen in figure 2.1. For $Re \ll 1$ it is referred to as *Stokes flow* and we can ignore inertial forces completely. This actually means that not only is the flow completely guaranteed to be laminar, but it is time reversible, meaning that reversing the flow any dynamics of the flow and particles in the flow will revert perfectly as well [15].

Turbulent



Laminar

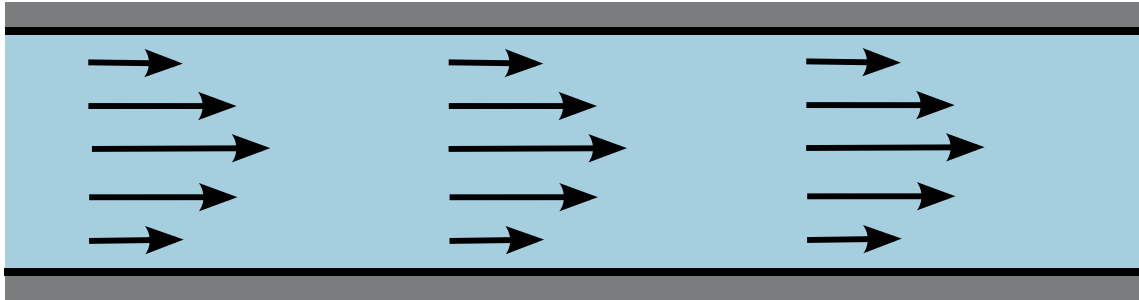


Figure 2.1: This shows the principal difference between laminar and turbulent flow.

2.1.3 Stokes Drag and Stokes's law

The drag force F_D exerted by a fluid on a spherical particle for $Re \ll 1$ is found using the so called Stokes's law [16]

$$F_D = 6\pi\mu Rv \quad (2.2)$$

where v is the velocity of the sphere relative to the fluid, μ is the dynamic viscosity and R is the radius of the sphere. The terminal velocity of the sphere is found by equating the gravitational force F_G acting on the sphere with the drag force. F_G is

$$F_G = \Delta\rho g \cdot \frac{4\pi R^3}{3} \quad (2.3)$$

where $\Delta\rho$ is the difference in density and g is the specific gravity. We find that the terminal velocity of a sinking (or floating) sphere is

$$v_s = \frac{2}{9} \frac{\Delta\rho}{\mu} g R^2 \quad (2.4)$$

2.2 Euler Angles and our Coordinate System

When describing rotating particles it is common to use the so called Euler Angles. A formal definition can be found at MathWorld [17] but for the purposes of this thesis we will describe it as a transformation from our stationary coordinate system $\{x,y,z\}$ to the coordinate system attached to our particle $\{x',y',z'\}$. This transformation is done in three steps and using the intermediate axis T.

- Rotate the x-y plane ϕ about the z-axis.
- Denote the shifted x axis T and rotate the z-y' plane θ around this axis
- Rotate ψ around the z' axis to obtain the final coordinate system

This is illustrated in figure 2.2 where each prim marks one more step of rotation to the coordinate system. To make it clear how this relates to the experiment figure 2.3 shows the Euler angle rotations for a triaxial particle shown from a point of view similar to the of the experiment where the X-Z plane is the primary plane. This means we can describe the orientation of a particle using $\mathbf{E} = (\phi, \theta, \psi)$.

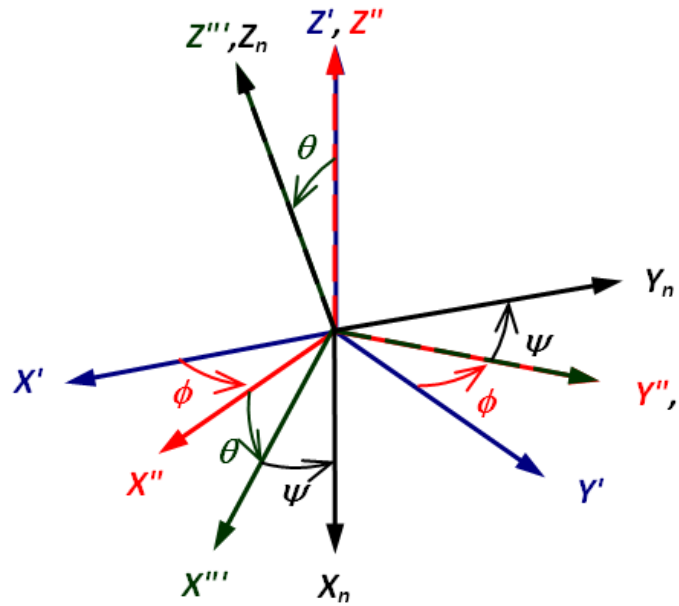


Figure 2.2: The Euler angles illustrated using a series of coordinate rotations. This is the normal way of illustrating the Euler angles as it is how they are defined.

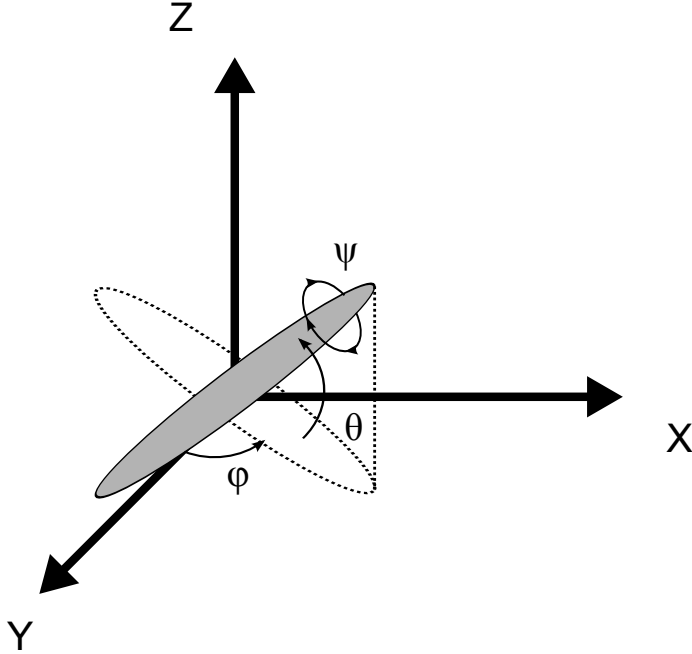


Figure 2.3: The Euler angles illustrated using an ellipsoid. This alternate visualization shows the angles with a point of view similar to that of the camera in the experiment. Note although ψ has an impact on the particle dynamics, as the particle is nearly axis-symmetric we can not observe it

2.2.1 Triaxial particles

Triaxial particles have, as the name suggests, three axis which are all distinct, compared to a sphere which has only one and an ellipse that has two. I will in this thesis refer to the lengths of these axes as a_x, a_y, a_z corresponding to their lengths along those axes for $\mathbf{E} = (0,0,0)$.

When discussing triaxial particles that are close to being axissymmetric or ellipsoids of the form $a_x \ll a_y \approx a_z$ it is convenient to introduce the particle asymmetry ϵ defined as

$$\epsilon = \frac{a_y}{a_z} - 1 \quad (2.5)$$

and the aspect ratio λ given by

$$\lambda = \frac{a_x}{a_y}. \quad (2.6)$$

2.3 Jeffery Orbits

The Jeffery Orbits describe the motion of an ellipsoidal particle in stokes shear flow as a function of time. The initial orbits found by Jeffery were for axis-symmetrical ellipsoidal particles, but was generalized by Yarin et al [7] to triaxial particles. Note that Jeffery Orbits sometimes refers only to the symmetric orbits but I will in this thesis refer to the generalized orbits as the Jeffrey Orbits. The generalized equations of motion found by Yarin et al was

$$\frac{d\theta}{dt} = (g_2 \sin \psi + g_3 \cos \psi) \sin \theta \quad (2.7a)$$

$$\frac{d\phi}{dt} = \frac{1}{2} + g_3 \sin \psi - g_2 \cos \psi \quad (2.7b)$$

$$\frac{d\psi}{dt} = g_1 + (g_2 \cos \psi - g_3 \sin \psi) \cos \theta \quad (2.7c)$$

$$(2.7d)$$

where the functions g_i are defined as

$$g_1 = \frac{a_y^2 - a_z^2}{2(a_y^2 + a_z^2)} \left(-\frac{1}{2}(\cos^2 \theta + 1) \sin 2\phi \sin 2\psi + \cos \theta \cos 2\phi \cos 2\psi \right), \quad (2.8a)$$

$$g_2 = \frac{a_z^2 - a_x^2}{2(a_x^2 + a_z^2)} \left(-\cos \theta \sin 2\phi \sin \psi + \cos 2\phi \cos \psi \right), \quad (2.8b)$$

$$g_3 = \frac{a_x^2 - a_y^2}{2(a_x^2 + a_y^2)} \left(\cos \theta \sin 2\phi \cos \psi + \cos 2\phi \sin \psi \right) \quad (2.8c)$$

. The Euler angles (ϕ, θ, ψ) are defined as can be seen in figure 2.2.

Solutions to the equations of motions can be found with numerical methods as shown by [7] but one has to be careful to convert to the right coordinates.

The time evolution of θ and ψ for different initial conditions can be plotted in a Poincaré map, also known as a Surface of Section (S.O.S) [18] for $\phi = 0$. The points for every initial condition is bound to a certain region of such a map called the orbit. A few such maps can be seen in figure 2.5

2.3. JEFFERY ORBITS

For a particle with a small $\epsilon \in [0.01 - 0.05]$ there are essentially three classes of orbits.

1. **Periodic:** For larger $|\theta|$ there is little variation and the particle is largely periodic with fluctuations too small to measure.
2. **Quasi-periodic bent:** For intermediate $|\theta|$ the amplitude of $\cos(\theta)$ changes noticeably but does not change sign.
3. **Quasi-periodic circular:** For small $|\theta|$ the amplitude of $\cos(\theta)$ will change noticeably and change sign from positive to negative.

For larger asymmetries $\epsilon < 0.05$ there will also be chaotic orbits that will appear as areas with dots. Such orbits can be seen in figure 2.5d.

These three different types of orbits are illustrated in figure 2.4 both on the S.O.S. as well as the components of \mathbf{n} . We can see that while n_x and n_y are periodic but with different amplitudes the behaviour for n_z is significantly different. For the large n_z orbit shown in green there is very little variation over time, only a slight modulation. For the bent quasi periodic orbit in red there is a far more significant modulation with a fixed period and for the circular quasi periodic orbit in blue n_z changes sign.

2.3. JEFFERY ORBITS

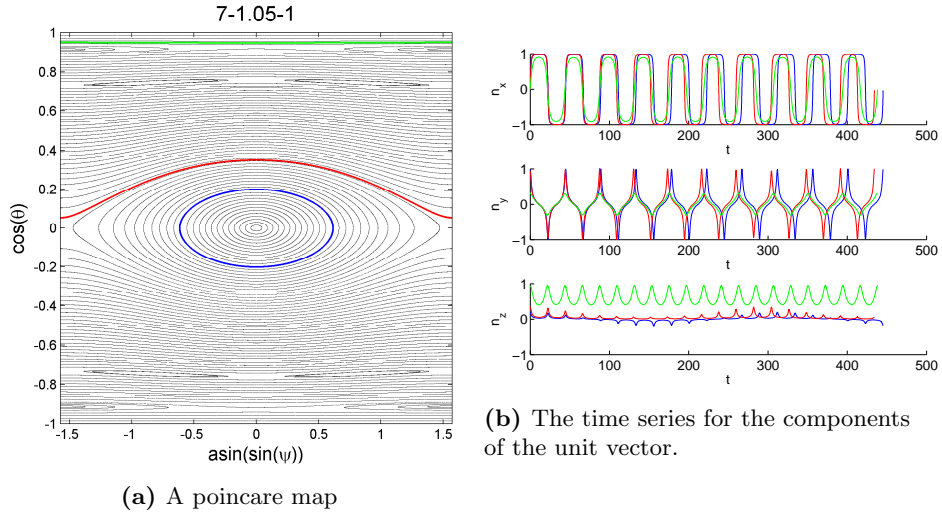


Figure 2.4: A poincaré map and three orbits for the Jeffery orbits of a particle with $\lambda = 7$ and $\epsilon = 0.05$. The three orbits highlight the three different kinds of orbit, the quasi periodic circular orbit in blue, the quasi-periodic bent orbit in red and the periodic in green. We see that while n_x and n_y look qualitatively similar but differ in amplitude for the different orbits n_z shows three different types of behaviour

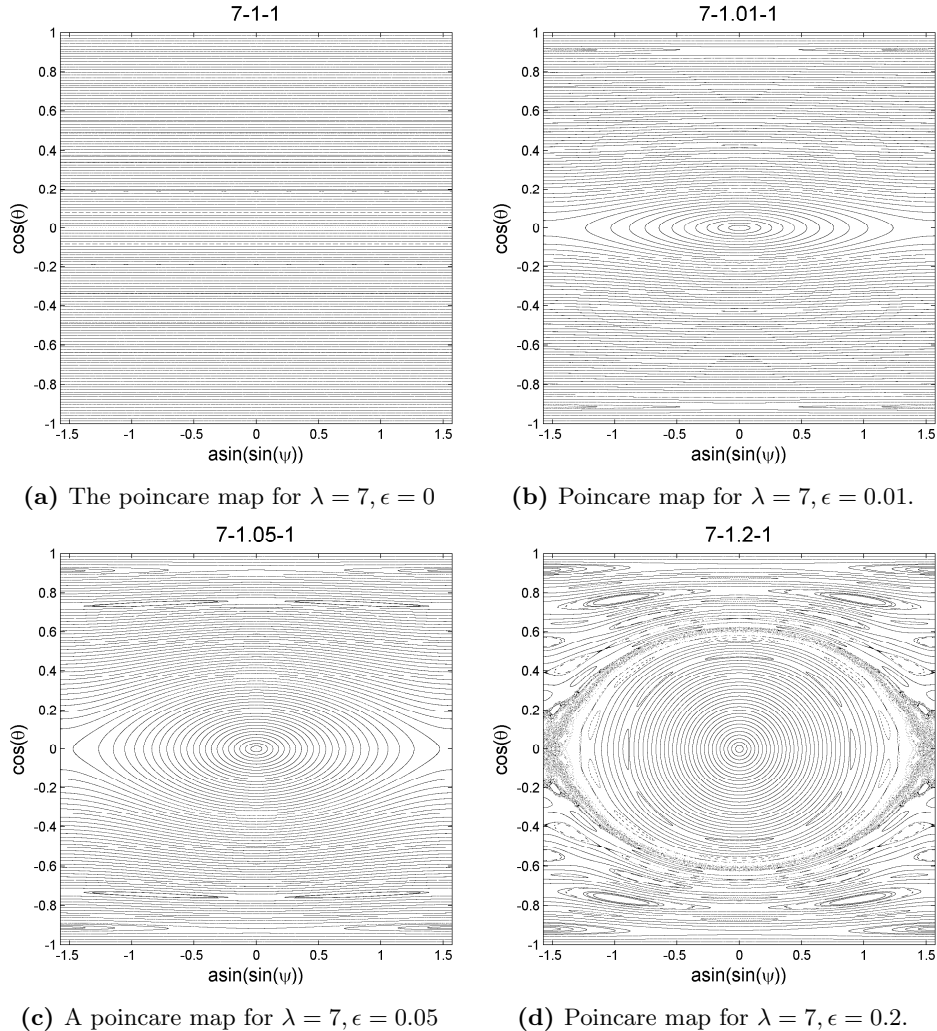


Figure 2.5: Four Poincare maps for different ϵ . Already at $\epsilon = 0.01$ there are noticeably quasi-periodic orbits around the center but it is also significantly larger for $\epsilon = 0.05$. For $\epsilon = 0.2$ we can see chaotic orbits around the center orbits that appear as a ‘sea’ of dots.

2.3.1 Winding Number

The quasi-periodic orbits are also referred to as double-periodic in, for example in Yarin [7]. This is referring to the fact that the variations that are seen in figure 2.4b are periodic as well. The ratio

between the two periods is referred to as the winding number ω , or simply

$$\omega = \frac{\theta_1}{\theta_2}. \quad (2.9)$$

which is illustrated in figure 2.6.

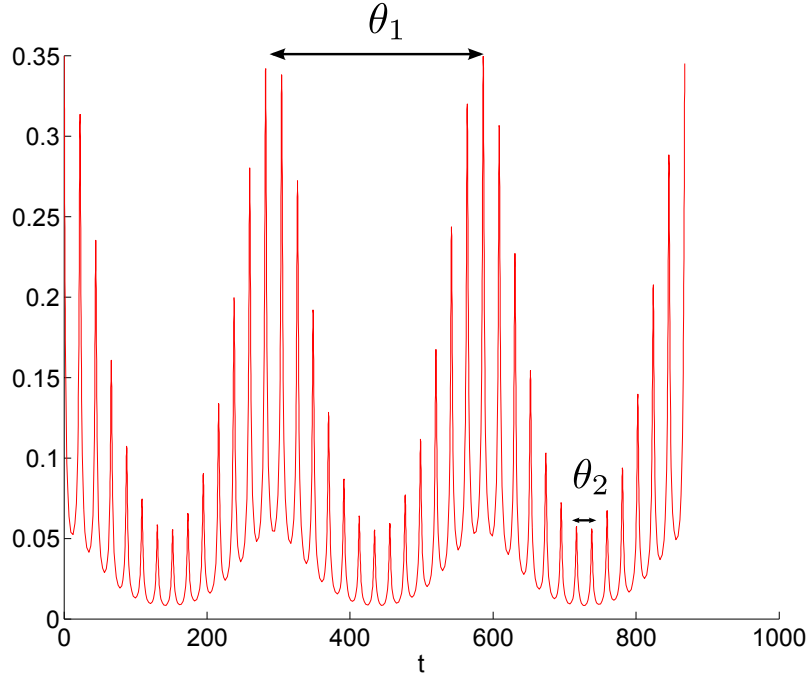


Figure 2.6: The winding number is defined as the quotient between the longer and shorter period. This is the n_z plot bent quasi periodic orbit from figure 2.4 highlighting the short period θ_2 which is simply the period of ϕ and the longer period θ_1 .

This can also be thought of as the number of steps travelled on the poincare map before coming back to where it started, divided by the number of laps it takes. This number is the same for any point along a given orbit on the poincare map but varies greatly for different orbits as well as for different asymmetries. The winding numbers for orbits a slice along $\psi = 0$ for $\epsilon = \{0.01, 0.05, 0.10\}$ can be seen in figure 2.7 which means that if we can measure the winding number we should be able to approximate the asymmetry of the particle fairly well, especially if we can see the gap between a quasi periodic bent orbit and a circular orbit.

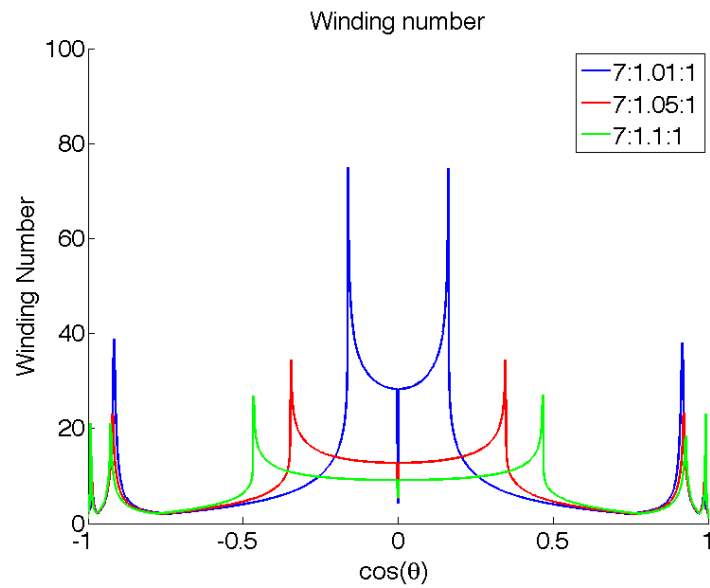


Figure 2.7: The winding number as a function of $\cos(\theta)$ for three different asymmetries. The sharp edge that occurs centered around zero is where the circular orbits change into bent orbits. We see that a lower asymmetry leads to a sharper difference between the circular and the bent orbits.

3

Method

Part I

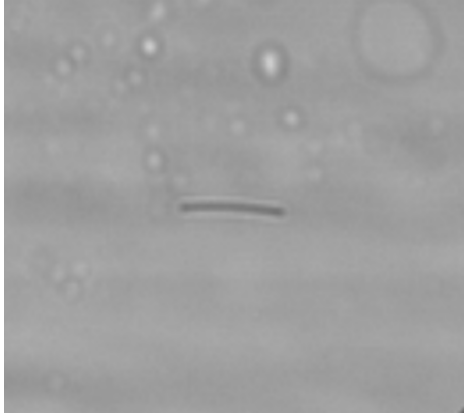
Improvements of Experimental Setup

As previously mentioned this thesis is a continuation of work done by Mehlig, Einarsson and Mishra et al [1, 13, 19]. Their results were promising but there were a number of key limitations and problem that we want to solve to improve the results and the ease of getting results. They can be summarized as:

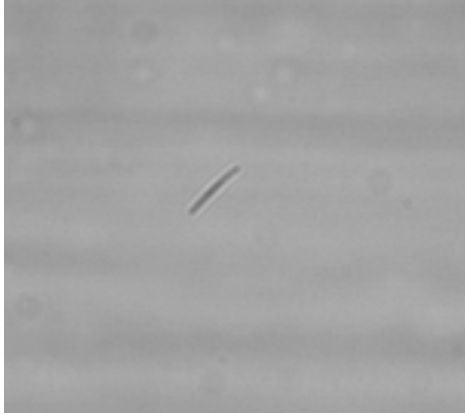
1. The particles
 - Very few particles are symmetric, most are visibly bent or uneven, see figure 3.1
 - The average aspect ratio is very high which means there will be very few flips along a stretch.
 - The width cannot be measured and is not uniform which makes estimates of the aspect ratio hard.
 - Cannot be trapped with an optical tweezer due to low transmittance.
2. The PDMS in the channel is very jagged which causes a great deal of noise unless the focus is in a very narrow band
3. Manual tracking of particles is time consuming and mentally draining.
4. Bubbles are difficult to avoid when setting up the experiment

3.1 Improvements

3.1.1 Particles and Channel



(a) Particle 13 from July 2012



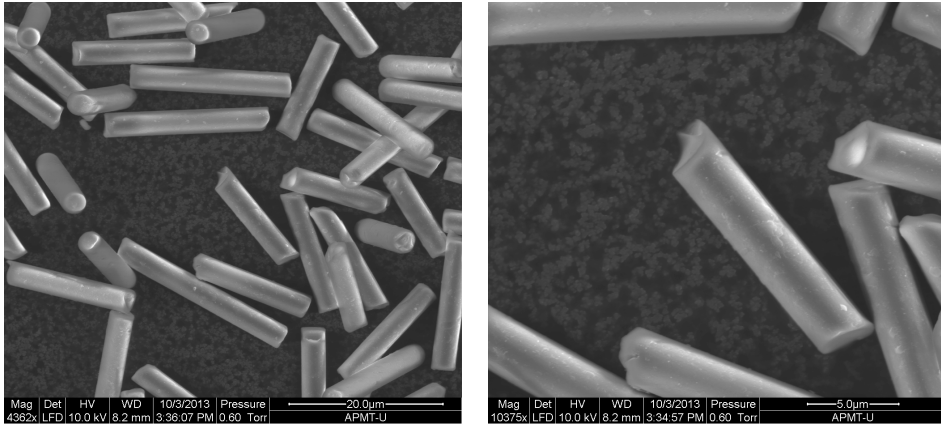
(b) Particle 22 from July 2012

Figure 3.1: Two fairly typical particles from the previous setup. Note that these are still selected from the total pool of particles for being relatively symmetric and yet are noticeably bent.

To solve the problems with the particles we replaced them with glass particles from Nippon Glass, Japan [20]. The particles are made from LCD spacing rods that are , which means they are essentially broken cylinders with very consistend width but quite varying length. Two different batches of particles have been used, one with $3\mu m$ diameter and one batch with $5\mu m$ diameter. All the particles presented in the results section are from the $3\mu m$ batch. To verify that the particle were indeed as symmetric and with as even width as we suspected images were taken with an ESEM (Environmental Scanning Electron Microscope) and can be seen in figure 3.2. We see that the particles are uniformly smooth along the edges but have varyingly jagged edges causing different degrees of asymmetry.

In particular figure 3.3b shows a top down view of a particle clearly showing a very circular shape with no discernible asymmetry.

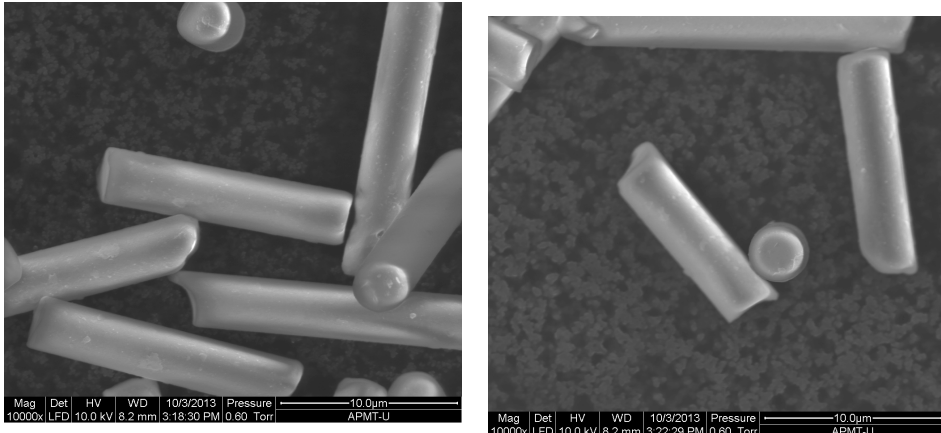
3.1. IMPROVEMENTS



(a) Shows a detailed view of a number of particles.

(b) Shows in detail the jagged edge of a particle.

Figure 3.2: Pictures of the glass particles that were used. Their width is highly uniform and there is a noticeable variance in asymmetry. Some particles show very clearly jagged edges while others appear very smooth which suggests they should have quite different ϵ and then exhibit quite different behaviour.



(a) What appears to be a highly symmetric particle.

(b) A top down view of a particle.

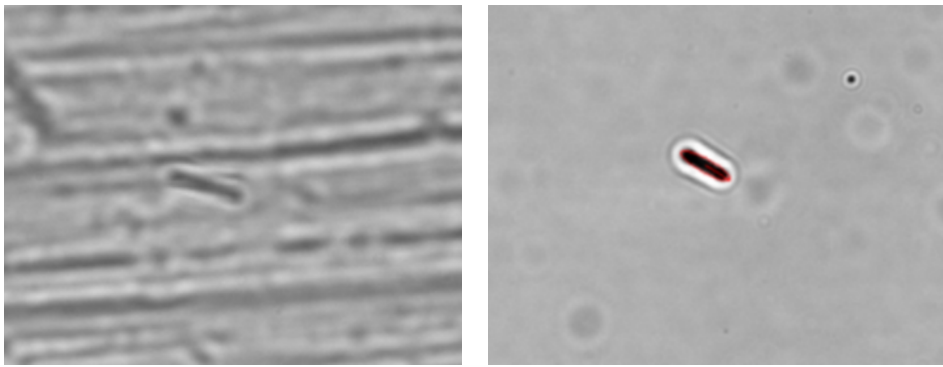
Figure 3.3: Pictures highlighting the roundness of the particles as well as the apparent symmetry of some particles. It should be noted that although there are no apparent rough edges there was no way to rotate a sample so there might very well be asymmetries on the side of the particle that we cannot see.

While these particles seemingly satisfy the symmetry conditions they are made of glass with a density of approximately 2.57 g/cm^3 at 20°C which is significantly higher than that of water with a

3.1. IMPROVEMENTS

density of 1 g/cm^3 at 20 C° and glycerol with a density of 1.5 g/cm^3 . Thus to correct for the density and limit sinking or floating the water soluble Sodium metatungstate which at 20 C° has maximum density of 2.94 g/cm^3 . To increase the viscosity of the liquid around 8% glycerol is added and the liquid was measured using a MCR 302 rheometer to have a dynamic viscosity of $24 \cdot 10^{-3}\text{ Pa s}$.

A problem in finding and tracking a particle was that the surface of the PDMS was very uneven and one could see sharp ridges along the length of the channel like in figure 3.4a unless the focus was in a relatively narrow depth of the channel.



(a) An unusual severe case of the PDMS edges creating noise. (b) After being polished there is no trace of such ridges.

Figure 3.4: Pictures highlighting the roundness of the particles as well as the apparent symmetry of some particles. It should be noted that although there are no apparent rough edges there was no way to rotate a sample so there might very well be asymmetries on the side of the particle that we cannot see.

This was fixed by polishing the copper mold in which the PDMS channels are formed with a silicate abrasive (Autosol) and emery cloth. This reduces all visible scratches from the mold and thus from the PDMS and the result can be seen in figure 3.4b.

3.1.2 Automated Tracking

One of the most time consuming aspects as well as mentally draining is manually tracking a particle. Depending on the flow rate and the number of stretches and runs desired for a particle it can take several hours. Thus one of the primary targets for improvement as discussed by Johansson [1] was to try and make the camera tracking automatic. This would enable faster measurements as well as

3.1. IMPROVEMENTS

more measurements since it would reduce fatigue.

Such a tracking was implemented using Python and the external packages `OPENCV`, `NumPy`, `SciPy`, `ImageMagick` and `ctypes`. The goal of the tracking is relatively similar to the tracking described in ?? and more in detail in Johansson [1] however there are a few very important differences that produce unique problems.

3.1.3 Aquiring the image

The first step in this is to acquire the image from the microscope in order to identify (and track) the particle. However the Leica DFC350 FX camera only works with the proprietary Leica software which means there is no easy way to get this image straight from the camera in real time. This meant we were forced to use the `ImageGrabber` package in Python and then isolate the camera image from the screen. This quite easy to do but takes ca 50ms per frame which would be unnecessary for an open source camera software.

3.1.4 Removing noise

The first step is to reduce the static noise from the movie caused by dirt, scratches and other defects in the microscope and on the camera lens as can be seen in figure 3.8a. As the noise is static and everything else changes this is a simple matter of computing an average frame

$$\bar{F} = \frac{\sum_{n=1}^N F}{N} \quad (3.1)$$

an example of such an average frame can be seen in figure 3.8b. This is then removed from the camera frame and the result can be seen in figure 3.8c. After this we apply a smoothing function and Canny edge detection [?] and then use the resulting edge.

3.1.5 Contour detection and selection

Once an edge image has been generated, we use the OpenCV command, `Contours` which returns a list of every contiguous group of edge pixels. If we have chosen the threshold values to the edge detection correctly, this should include the particle or a good approximation of it.

In order to find the correct contour a few techniques are used.

First contours whose total size is less than some minimum value, n_{min} or larger than some maximum value n_{max} are ignored. Then the position P_i of each contour $C_i = p_1, p_2 \dots p_n$ is calculated as the average pixel position

$$P_i = \sum_j^n p_j / n$$

This position is compared to the expected position of the particle , which the very first frame is the middle position and thereafter is assumed to have constant speed.

Finally a 'thinness value' is calculated according to eq 3.2

$$w_{thin} \left(\frac{n}{d_{max}^2} \right)^2 \quad (3.2)$$

. where w_{thin} is a weighting constant, n is the number of pixels in the contour and d_{max} is the longest distance between two pixels in the contour.

3.1.6 Adjusting the Camera velocity

Once detected twice the particle will have some velocity relative to the camera v_{rel} and a position \mathbb{P} . If the velocity is larger than some threshold v_{thresh} or the position is outside a center square in the image, $\mathbb{P} \notin \mathbf{B}$ we want to adjust the velocity of the step engine.

We then simply do a straight correction but with a damping factor ζ to prevent a feedback loop. So our resulting velocity change V_c is

$$V_c = v_{rel} \cdot \zeta \quad (3.3)$$

3.1.7 Time Considerations

A higher frame rate will allow for greater predictive power and increase stability as the error between frames is reduced. So reducing computational time of each task is important for optimizing the tracking which also means knowing what tasks are the most demanding. A list of the different tasks and their average execution times can be seen in table 3.1

NOTE CURRENTLY NOT PUT IN ACTUAL DATA ONLY APPROXIMATE

Task	Average time	Std deviation
Capture screen	1000	200
Find edges	200	20
Change velocity	400	50

Table 3.1

We see that the FPS is limited primarily by three routines: The screen capture routine, the change velocity routine and finally the save position routine. The first and last are unavoidable and must be done every frame by definition if we are interested in knowing the particles position as well as possible. This means we simply want to use the velocity correction as little as possible. Since the time constraint is in the communication with the step engine, there is not any optimization to be done here, at least not within the scope of this thesis.

3.2 Experimental Setup

As the goal is to attempt to verify the Jeffrey equations in eq 2.7 we need an experimental setup with particles and flow system that satisfy the conditions during which the Jeffrey equations apply. This means our particles have to be buoyant, triaxially symmetric and the flow has to be Stokes flow.

Thus two sets of glass particles from Nippon Glass, Japan[20], have been used. They are cylindrical with a consistent width of $3\mu\text{m}$ and $5\mu\text{m}$ and varying length. Images taken with a

3.2. EXPERIMENTAL SETUP

STEM microscope can be seen in figure 3.2.

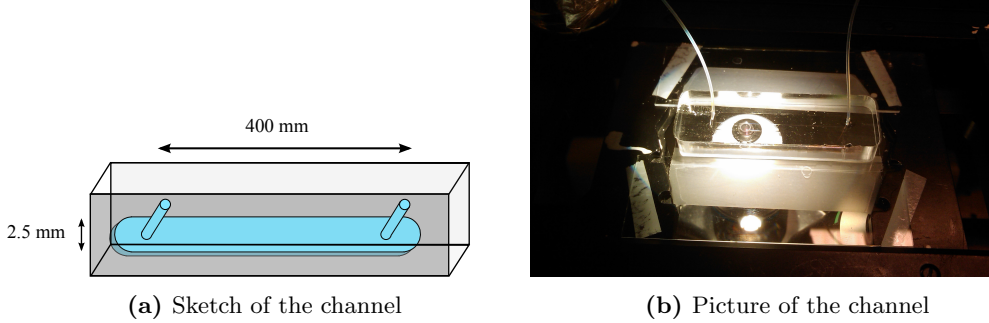


Figure 3.5

This liquid with suspended particles is flowed through a channel of Polydimethylsiloxane (PDMS) 4 cm long, 2.5 mm wide and either 200 μm and 500 μm . The flow profile of such a channel was calculated by Anton Johansson in his thesis[1] and can be seen in figure 3.6. The flow rate varies between 2 and 20 $\mu\text{l}/\text{m}$ or in SI units $3.33 \cdot 10^{-10} \text{ m}^3/\text{s}$ which with a cross section of at least $5 \cdot 10^{-7} \text{ m}^2$ means a maximum flow speed of 6.66 mm/s .

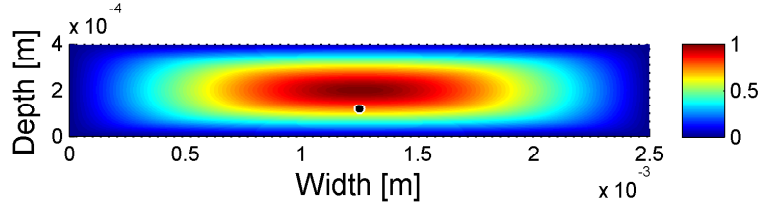


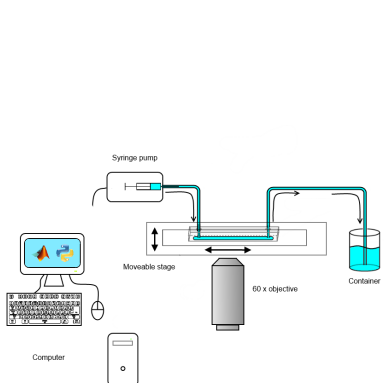
Figure 3.6: The theoretical estimation of the flow profile. Image used with permission from Johansson [1]

To confirm that the flow is a creeping flow we can calculate the maximum Reynolds number using eq 2.1 and our maximum flow speed

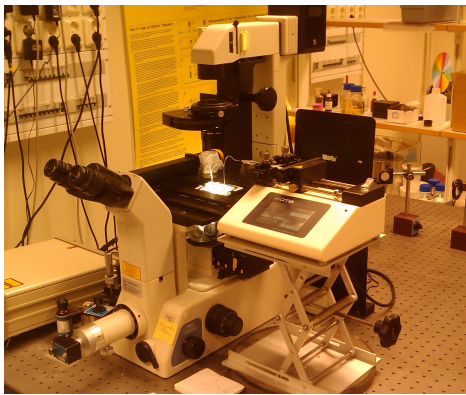
$$\text{Re} = \frac{UL\rho}{\mu} \leq \frac{6.66 \cdot 10^{-3} \cdot 2.5 \cdot 10^{-3} \cdot 2.5}{24 \cdot 10^{-3}} \approx 1.6 \cdot 10^{-3} \ll 1 \quad (3.4)$$

This should satisfy the conditions of the Jeffrey equations. To track the particles the channel is put in a moveable stage on a confocal microscope. The entire setup can be seen in figure 3.7

3.2. EXPERIMENTAL SETUP



(a) Sketch of the set up



(b) Overview of the set up

Figure 3.7

3.2.1 List of equipment

The equipment used during the experiment is as follows

- Leica DFC350 FX digital camera
 - Nikon Eclipse TE 300 microscope
 - Nikon 60x water immersion objective
 - Märzhäuser Wetzlar 'LStep-eco' step engine
 - CMA 4004 syringe pump

3.2.2 Density matching

$$\rho_a = \frac{m_a}{V_a} = \frac{V_b \rho_b + V_{mix} \rho_{mix}}{V_b + V_{mix}} \quad (3.5)$$

So if we want to find V_{mix} we get

$$V_{mix} = \frac{V_b(\rho_b - \rho_a)}{\rho_a - \rho_{mix}} \quad (3.6)$$

Part II

Measurements and Analysis

3.3 Data Analysis

Once a movie had been recorded we want to estimate the dynamics of the particle. This is done in several steps.

3.3.1 Particle identification

The first step is to reduce the static noise from the movie caused by dirt, scratches and other defects in the microscope and on the camera lens as can be seen in figure 3.8a. As the noise is static and everything else changes this is a simple matter of computing an average frame

$$\bar{F} = \frac{\sum_{n=1}^N F}{den} \quad (3.7)$$

an example of such an average frame can be seen in figure 3.8b. This is then removed from the camera frame and the result can be seen in figure 3.8c. After this we apply a smoothing function and Canny edge detection [?] and then fill the resulting edge. The resulting pixels are then fit to an ellipse as described in [1?]. The filled contour and the fit ellipse can be seen in figure 3.8d.

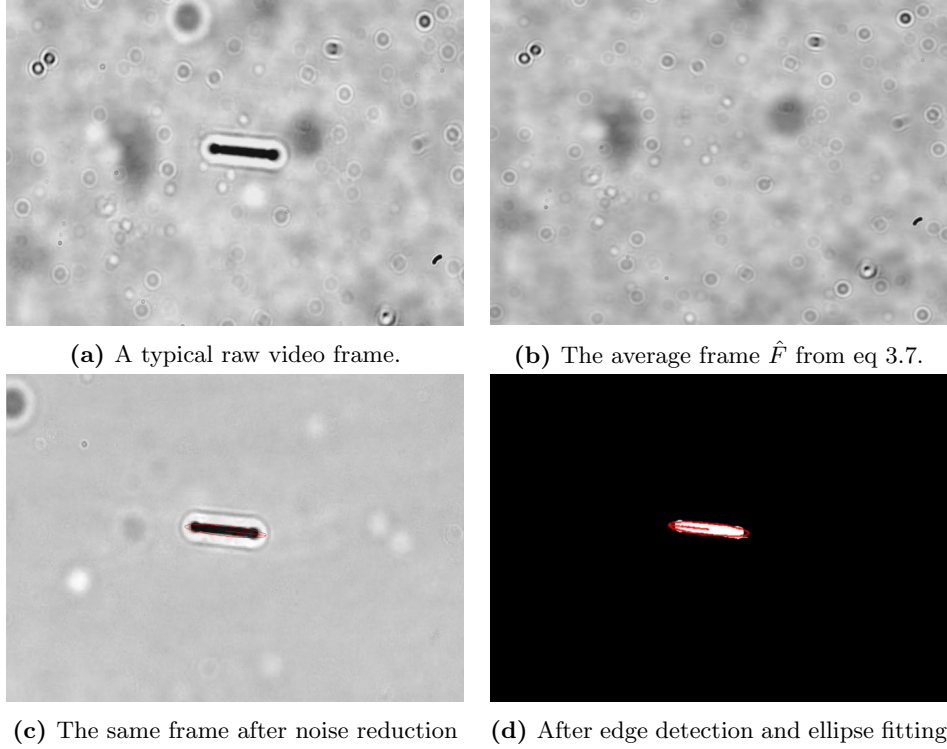


Figure 3.8: These pictures show a simplified version of the image analysis from raw image to estimated particle position

3.3.2 Estimation of orientation

The ellipsoid we get is then our best approximation of the projection of the actual particle. In order to normalize \mathbf{n} we need to know the length of the particle. However as it was shown by Leal that the particle will always spend a majority of its time aligned with the flow, ie aligned with the camera which means that by simply calculating the length L every frame and finding the mode of the distribution we will find a good estimate of L .

So given an ellipsoid with length l_e , width d_e and angle ϕ_p we find

$$p_x = l_e * \sin(\phi_p) \quad (3.8)$$

$$p_z = l_e * \cos(\psi_p) \quad (3.9)$$

with x and z projection p_x and p_z we can get n_x and n_z as well as n_y via

$$n_x = \frac{p_x}{L} \quad (3.10a)$$

$$n_z = \frac{p_z}{L} \quad (3.10b)$$

$$n_y = \sqrt{1 - n_x^2 - n_z^2} \quad (3.10c)$$

3.3.3 Width compensation

Up until this point we have assumed that the particle is a *thin* rod so that the projection \mathbf{p} onto the x and z-axes give us an accurate estimate of \mathbf{n} . However when we are projecting 'thick' particle with length L and width D we get \mathbf{n}' . At $\phi = 0$ this is

$$\mathbf{n}' = n'_z = n_z \cos(\theta) + D \sin(\theta) \quad (3.11)$$

which is illustrated in figure 3.9.

In order to compensate for this error we modify our projection equation 3.8 to

$$p_x = (l_e - w_e) * \sin(\phi_p) \quad (3.12)$$

$$p_z = (l_e - w_e) * \cos(\psi_p) \quad (3.13)$$

This will reduce the particles estimated length by w_e

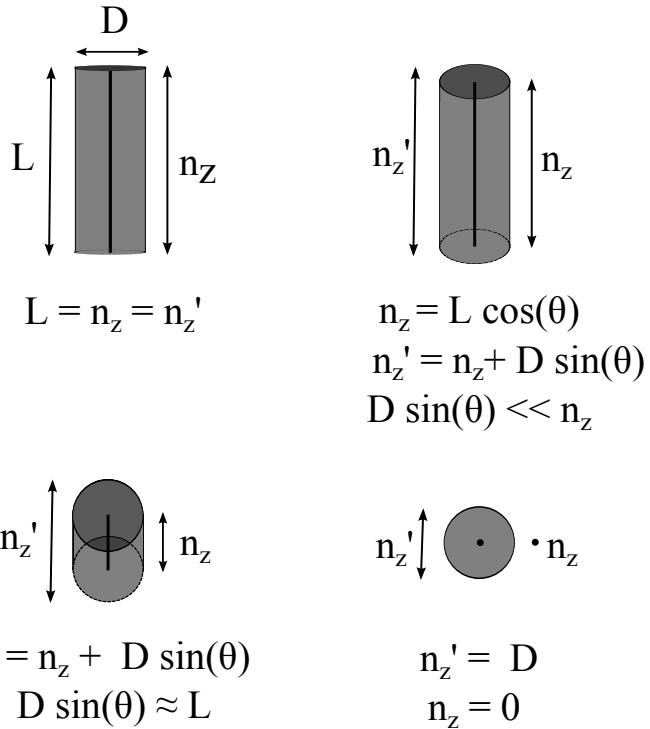
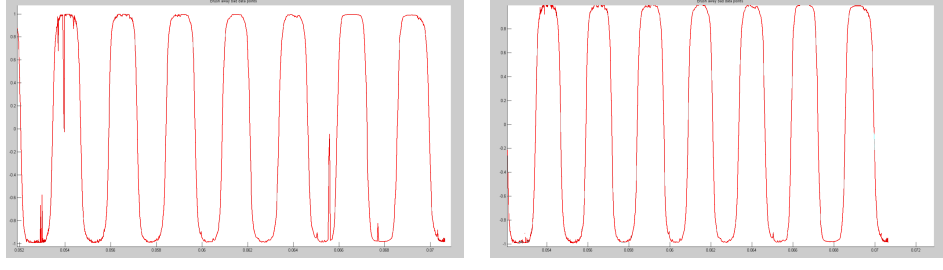


Figure 3.9

3.3.4 brushing

The tracking will typically have a few frames where either the particle is obstructed or is not detected correctly leading to spikes in the data. To make further theoretical analysis possible such points are removed manually. The basis for removal is simply a large discontinuity in the data, and while this could largely be eliminated with algorithmic means in particular for n_x it's very difficult to write an algorithm that will satisfactorily catch all possible edge cases. It's thus simpler to look at the analysis program and remove the points where the particle cannot be traced accurately due to noise.

An example of unbrushed and brushed data can be seen in figure 3.10 and all unbrushed data files will be available at [INSERTURLHERE](#)



(a) Tracking data before brushing. (b) tracking data after brushing.

Figure 3.10: Shows a set of data before and after removing points where a significant amount of noise disturbed the tracking.

3.3.5 Winding number estimation

As discussed in section 2.3.1, estimating the winding number for different types of orbit for one particle should allow for a rather accurate estimation of ϵ . So in order estimate the winding number for a measured particle we must identify where the θ_1 maxima and minima from figure 2.6 occur. The first step to do this is to find the θ_2 maxima which can be done quite easily by finding where $n_x = 0$. A plot of such points can be seen in figure ?? where we match each n_z peak with an index i . Unfortunately data is too noisy to allow for simple algorithmic approaches to finding good local maxima. Instead we select a number of maxima $M_1, M_2 \dots M_p$ with peak index $I_1^M, I_2^M, \dots, I_p^M$ and minima m_1, m_2, \dots, m_q with peak index $I_1^m, I_2^m, \dots, I_q^m$.

We can estimate the winding number \hat{w} as the average distance between the peak indices for the maxima and minima i.e.

$$\overline{d_M} = \frac{1}{p-1} \sum_{j=1}^p I_{j+1}^M - I_j^M \quad (3.14)$$

$$\overline{d_m} = \frac{1}{q-1} \sum_{j=1}^q I_{j+1}^m - I_j^m \quad (3.15)$$

$$\hat{w} = \frac{\overline{d_M} + \overline{d_m}}{2} \quad (3.16)$$

or in the case that we only have 1 maxima and minima we use instead

$$\hat{w} = |I_1^M - I_1^m| \cdot 2 \quad (3.17)$$

as the distance between maxima and minima should be half a period.

3.3.6 Matching to theoretical orbit

4

Results

During the work of this thesis around 300 movies of particles have been recorded with gradual improvements to the setup in terms of density matching, particle density, bubble elimination etc. In this section we will present the data from three movies of two different particles. One referred to as particle A, the other as particle B. The measurements in this section was done together with Alexander Laas.

4.1 Particle A

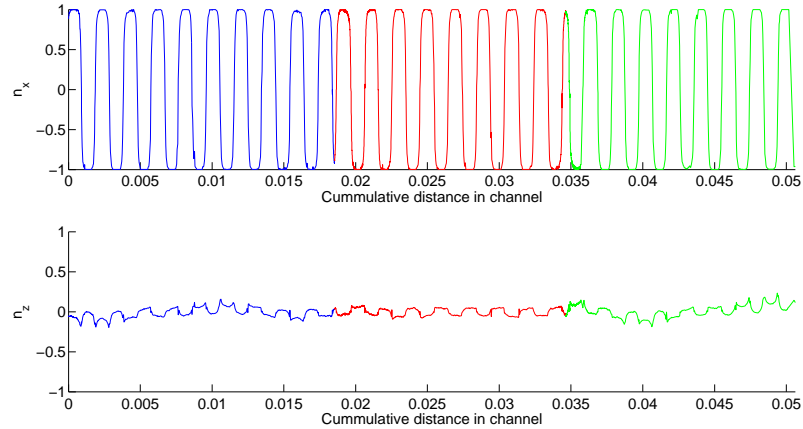


Figure 4.1: Despite being very close to a center orbit there is very little quasi periodic behaviour. The very flattened peaks compared to a low n_z orbit in 2.4b are a result of the width compensation discussed in section 3.3.3.

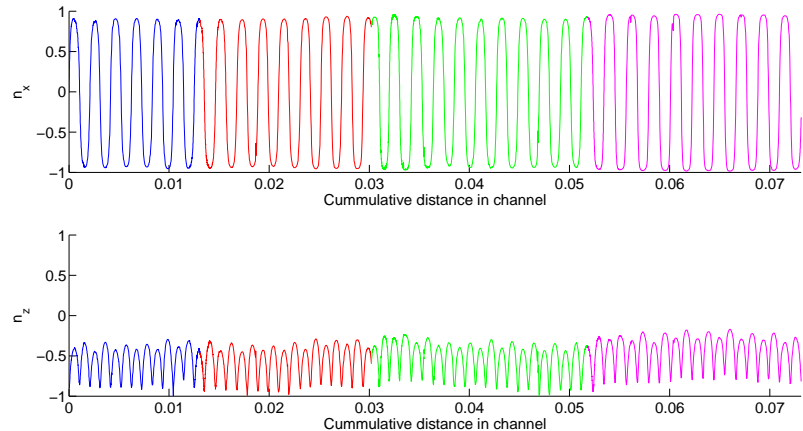


Figure 4.2: A tracked particle with a large n_z component with a very consistent periodic behaviour.

4.1. PARTICLE A

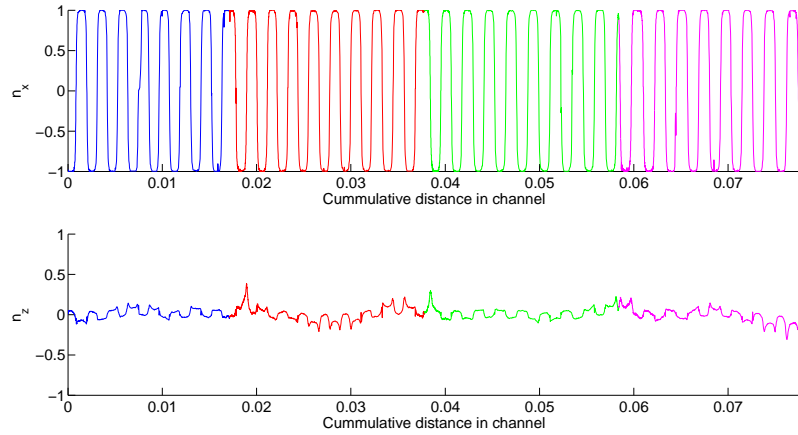


Figure 4.3: The peaks that occur after each reversal are not the cause of a tracking error but can be seen clearly in the films. The cause of such a sudden peak and then reverting back to another orbit is not known and we have no good theoretical explanation for it.

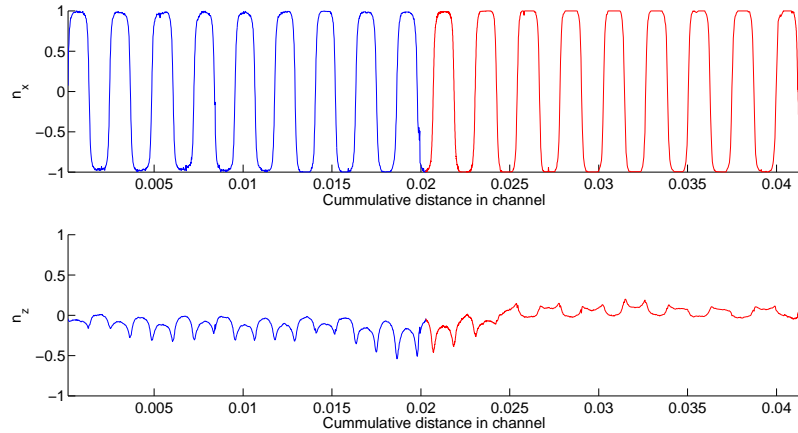


Figure 4.4: The flow is reversed when the particle is at (1) and we see that the orbit appears to change as well.

4.2 Particle B

4.2.1 Run 1

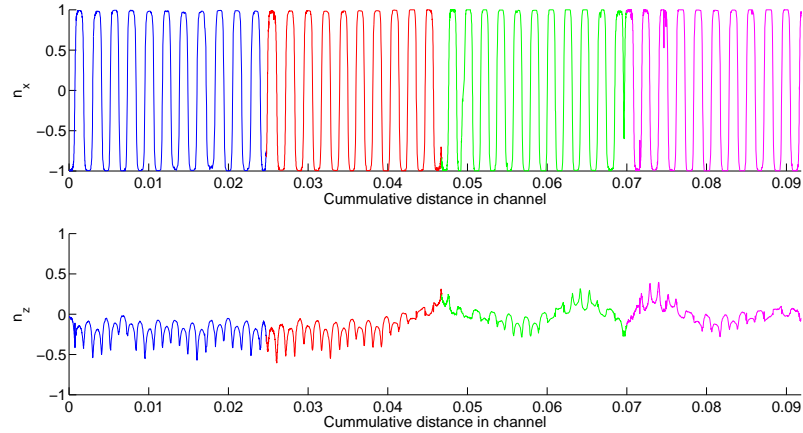


Figure 4.5: The first two stretches match very well as well as the last two. In the reversal between these two there is a large change which begins at (1) where the flow is starting to revert. This reversal also occurs at the end of the channel closer to the pump.

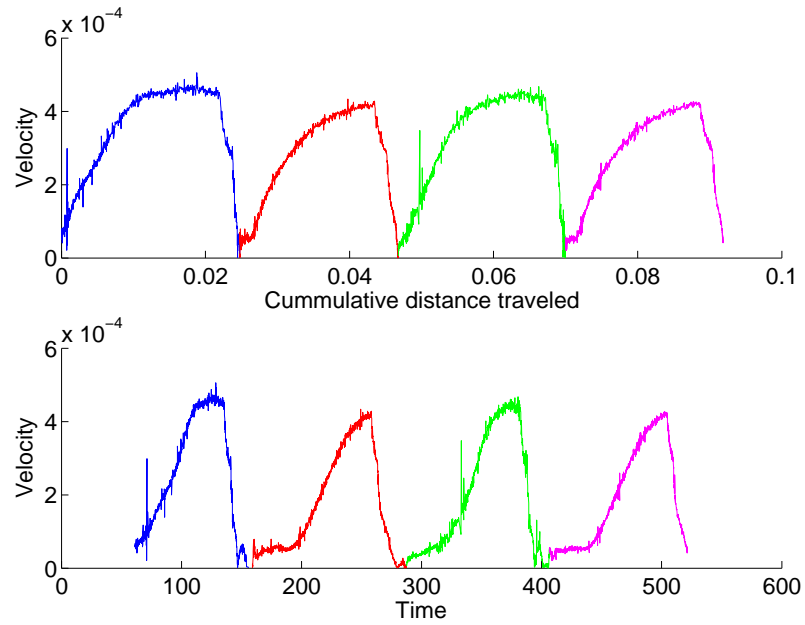


Figure 4.6: The speed of the particle against time and against position. In the plot against time there is an extra dip to 0 at around $t = 150$ and $t = 400$. This occurs only at the end of channel further away from the pump.

4.2.2 Run 2

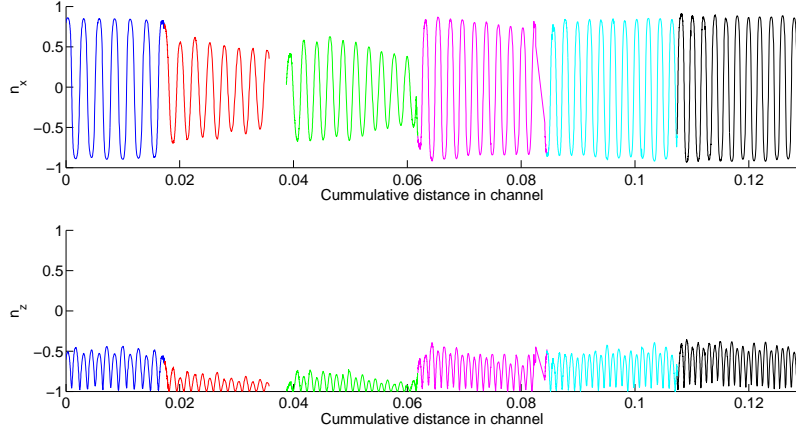


Figure 4.7: Mostly constant orbit for large n_z . The first and third reversal both change the orbit slightly but the size of the change is exaggerated by n_z being very close to 1. The actual change in orbit can be seen in figure ?? to not nearly as these plots suggest. Note also the missing data between the second and third stretch where the particle was lost in tracking for some time, as well as some missing data between the fourth and fifth stretch

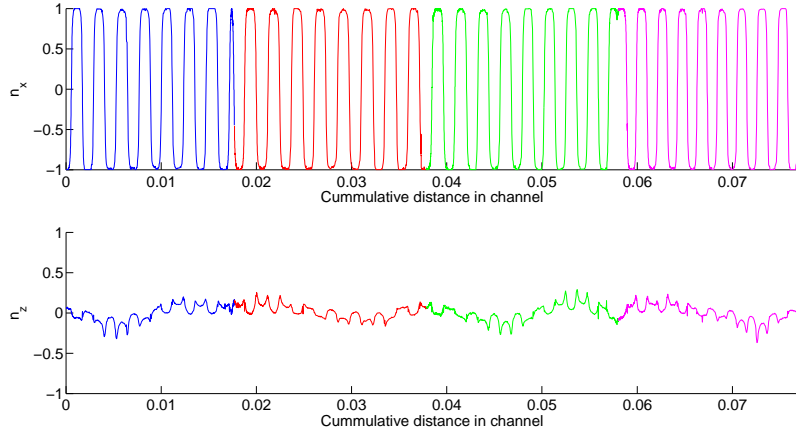


Figure 4.8: A circular quasi periodic orbit.

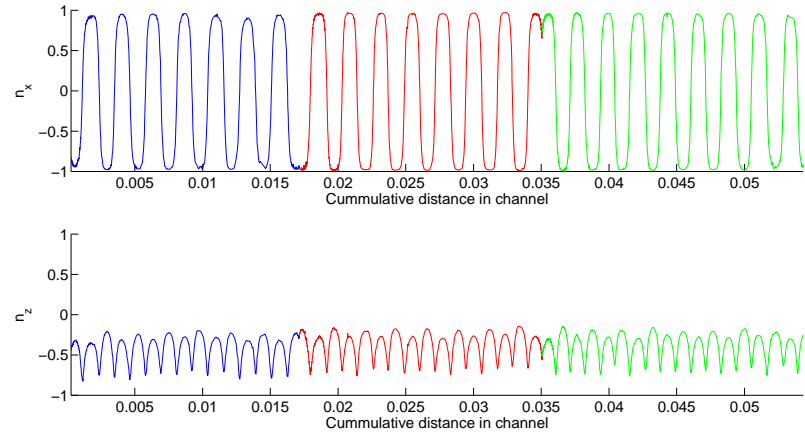


Figure 4.9: While there is not large change in n_z there seems to be some small variations that could correspond to a bent quasi periodic orbit.

5

Discussion

A

Raw data

Bibliography

- [1] J. A., Analysis of empirical data on the tumbling of microrods in a shear flow, Master's thesis, Chalmers University of Technology.
- [2] E. J., Low reynolds number particle dynamics, Master's thesis, Chalmers University of Technology.
- [3] A. Einstein, A new determination of molecular dimensions, Annalen der Physik.
- [4] G. B. Jeffrey, The motion of ellipsoidal particles immersed in a viscous fluid, Proceedings of the Royal Society A 102.
- [5] P. J. Gierszewski, C. E. Chaffey, Rotation of an isolated triaxial ellipsoid suspended in slow viscous flow, Canadian Journal of Physics 56 (1) (1978) 6–11.
- [6] L. G. L. E. J. Hinch, Rotation of small non-axissymmetrical particles in a simple shear flow, J. Fluid Mech 92 (1979) 591–608.
- [7] I. V. R. A. L. Yarin, O. Gottlieb, Chaotic rotation of triaxial ellipsoids in simple shear flow, J. Fluid Mech vol 340 (1997) 83–100.
- [8] F. C. van den Bosch, lecture 1: Surfaces of section, Online material for course.

BIBLIOGRAPHY

- [9] S. G. M. H. L. Goldsmith, The flow of suspensions through tubes i. single spheres, rods, and discs, Jounrla of colloid science (17).
- [10] D. K. O.G. Harlen, Orientational drift of a fibre suspended in a dilute polymer solution during oscillatory shear flow, *J. Non-Newtonian Fluid Mech.* 73 (1997) 81–93.
- [11] T. Kaya, H. Koser, Characterization of hydrodynamic surface interactions of escherichia coli cell bodies in shear flow, *Phys. Rev. Lett.* 103 (2009) 138103.
- [12] C. J. S. Petrie, The rheology of fiber suspensions, *J. of non-newtonian fluid mechanics* 87.
- [13] J. E. et al, Periodic and aperiodic tumbling of microrods advected in a microchannel flow, *Acta Mechanica* (2013) 1–9.
- [14] T. Pedley, *Introduction to Fluid Dynamics*, Department of Applied Mathematics and Theoretical Physics, University of Cambridge, Silver St., Cambridge CB3 9EW, U.K., 1997.
- [15] S. Childress, *An Introduction to Theoretical Fluid Dynamics*, Cambridge University Press, 2008, page 117 Starts the discussion of time reversibility of Stokes' Flow.
URL www.math.nyu.edu/faculty/childres/fluidsbook.pdf
- [16] G. K. Bachelor, *An Introduction to Fluid Dynamics*, Cambridge University Press, 1967, page 212 is definition of Reynolds Number, page 233 is Stokes Law.
- [17] W. E. W, Euler angles, from MathWorld—A Wolfram Web Resource. (2013).
URL <http://mathworld.wolfram.com/EulerAngles.html>
- [18] J. Munkhammar, Poincare map (2013).
URL mathworld.wolfram.com/PoincareMap.html
- [19] J. E. e. a. Y. N. Mishra, A microfluidic device for studies of the orientational dynamics of microrods, *Proc. SPIE* 8251 2825109.
- [20] N. E. G. Co, Gap spacers for lcds: Microrods, www.neg.co.jp/epd/elm/e_prd/other/others_01.pdf.